

How wind shear affects trade-wind cumulus convection

K. C. Helfer¹, L. Nuijens¹, S. R. de Roode¹, A. P. Siebesma^{1,2}

¹Department of Geoscience and Remote Sensing, Delft University of Technology, Delft, The Netherlands

²Royal Netherlands Meteorological Institute (KNMI), De Bilt, The Netherlands

Key Points:

- Shear in the zonal wind influences cloud-top heights via the effect of momentum transport on the surface wind and surface fluxes.
- Backward shear (surface easterlies turn westerlies) lowers cloud tops and shallows and moistens the trade-wind layer.
- Any absolute amount of wind shear limits in-cloud updraft speeds and enhances low-level cloud fraction.

Corresponding author: Kevin Helfer, k.c.helfer@tudelft.nl

Abstract

Motivated by an observed relationship between marine low cloud cover and surface wind speed, this study investigates how vertical wind shear affects trade-wind cumulus convection, including shallow cumulus and congestus with tops below the freezing level. We ran large-eddy simulations for an idealised case of trade-wind convection using different vertical shears in the zonal wind. Backward shear, whereby surface easterlies become upper westerlies, is effective at limiting vertical cloud development, which leads to a moister, shallower and cloudier trade-wind layer. Without shear or with forward shear, shallow convection tends to deepen more, but clouds tops are still limited under forward shear. A number of mechanisms explain the observed behaviour: First, shear leads to different surface wind speeds and, in turn, surface heat and moisture fluxes due to momentum transport, whereby the weakest surface wind speeds develop under backward shear. Second, a forward shear profile in the subcloud layer enhances moisture aggregation and leads to larger cloud clusters, but only on large domains that generally support cloud organization. Third, any absolute amount of shear across the cloud layer limits updraft speeds by enhancing the downward-oriented pressure perturbation force. Backward shear — the most typical shear found in the winter trades — can thus be argued a key ingredient at setting the typical structure of the trade-wind layer.

Plain Language Summary

We used a high-resolution weather model to investigate the influence of the shape of the wind profile (i.e. whether the wind blows faster, slower or with the same velocity at greater altitudes compared to the surface) on shallow cumulus clouds typical of the North Atlantic trade-wind region. In this region, easterly winds that decrease with height (and eventually turn westerly) are most common. Generally, the surface winds are also affected by how the wind blows further aloft, influencing what kind of clouds form. But even when we eliminate this effect in our study, we find that when the wind blows faster or slower at greater heights, clouds are not only tilted but also wider, and both effects increase the overall cloud cover. Furthermore, if the wind speed changes with height, the updraft speed within clouds is diminished, which potentially decreases the height of clouds. However, if the wind speed increases with height (which only rarely occurs in the trades), clouds tend to cluster more, which ‘offsets’ the weaker updrafts, and thus still allows for deeper clouds.

1 Introduction

In light of the uncertain role of trade-wind cumulus clouds in setting the cloud feedback in climate change, there is widespread interest in understanding the behaviour of these clouds, the different ways they interact with their environment and how this changes in response to global warming (e.g. Bony & Dufresne, 2005; Bony et al., 2013; Vial et al., 2017). Trade-wind cumuli are found in regions characterised by the trade winds, yet we understand relatively little about how they depend on the structure of the trade wind, compared to how they depend on temperature and moisture. Some studies have investigated the influence of the wind speed on low clouds in the trades and revealed that surface wind speed is one of the better predictors of low cloud amount (e.g. Nuijens & Stevens, 2012; Brueck et al., 2015; Klein et al., 2017). But it is unclear how much the wind shear plays a role in observed cloud amount–wind speed relationships, as one might expect both wind speed and wind shear to increase with larger meridional temperature gradients throughout the lower troposphere when assuming geostrophic and thermal wind balance. Furthermore, little work has concentrated on the influence of wind shear on convection, other than its role in increasing the amount of projected cloud cover.

From studies of deep convection we know that wind shear can have a number of effects. Shear is effective at organizing deep convective systems into rain bands and squall lines (e.g. Thorpe et al., 1982; Rotunno et al., 1988; D. J. Parker, 1996; Hildebrand, 1998; Robe & Emanuel, 2001; Weisman & Rotunno, 2004). At the same time, shear can limit convection during its developing stages (Pastushkov, 1975). A recent paper by Peters et al. (2019) clearly shows how shear reduces updraft speeds in slanted thermals by enhancing the (downward-oriented) pressure perturbations. Shear is also argued to inhibit deep convection by ‘blowing off’ cloud tops (e.g. Sathiyamoorthy et al., 2004; Koren et al., 2010), which we interpret as an increase in the cloud surface area that experiences entrainment, which also plays a role in setting updraft buoyancy and updraft speeds.

Malkus (1949) might have been one of the first to mention the effect of shear on shallow convection, noting that the tilting of clouds through shear causes an asymmetry in its turbulence structure with more turbulence on the windward than the leeward side. Through numerous studies we now know that shear helps organize shallow convective clouds in rolls or streets along with the development of coherent moisture and temperature structures in the subcloud layer (e.g. Malkus, 1963; Asai, 1964; Hill, 1968; LeMone

76 & Pennell, 1976; Park et al., 2018). Li et al. (2014) explain how shear over the subcloud
77 layer interacts with the low-level circulation induced by cold pools to enhance or limit
78 the regeneration of convective cells and longevity of shallow cloud systems. In a recent
79 LES study of shallow convection over the Sulu Sea in the Philippines, Yamaguchi et al.
80 (2019) find that wind shear leads to a stronger clustering of clouds and slightly increased
81 cloud-base cloud fractions as well as diminished cloud depths. Brown (1999) shows that
82 shear can strongly affect the surface wind via momentum transport, but that it has lit-
83 tle effect on the turbulence kinetic energy (TKE) budget, on scalar fluxes and on cloud
84 properties. This is in contrast to the dry convective boundary layer, where shear has a
85 strong impact on the TKE budget (Fedorovich & Conzemius, 2008, and references therein).

86 The present study investigates how vertical wind shear influences trade-wind cu-
87 mulus convection, including shallow cumulus and cumulus congestus below the freezing
88 level. For instance, we ask, how shear impacts cloud tops, cloud amount and the struc-
89 ture of the boundary layer. To this end, we used an idealised large-eddy-simulation (LES)
90 case — inspired by Bellon and Stevens (2012) and Vogel et al. (2016) and not unlike the
91 typical atmosphere in the trades — aiming at a fundamental understanding of the sen-
92 sitivity to forward and backward shear (by which we mean an increase and decrease, re-
93 spectively, of the zonal wind speed with height) of different strengths.

94 The remainder of this paper is structured as follows. We first explain our idealised
95 LES set-up and the wind shear variations we impose. The results are then presented in
96 a twofold manner. First, we discuss the effects of shear on the cloud and boundary-layer
97 evolution, showing results from large- and small-domain simulations with interactive and
98 prescribed surface fluxes. Second, focusing on the large-domain runs with constant sur-
99 face fluxes, we discuss how shear impacts the cloud structure and cloud depth without
100 surface flux responses. We end with a concluding discussion and an outlook on future
101 work. In an appendix, we discuss the influence of shear on the clouds' vertical-velocity
102 budget.

103 **2 Experimental design**

104 We carried out large-eddy simulations (LES) using version 4.2 of the Dutch Atmo-
105 spheric Large Eddy Simulation (DALES; Heus et al., 2010). In our experimental set-up,
106 we prescribed large-scale forcings and initial profiles typical of the North Atlantic trades

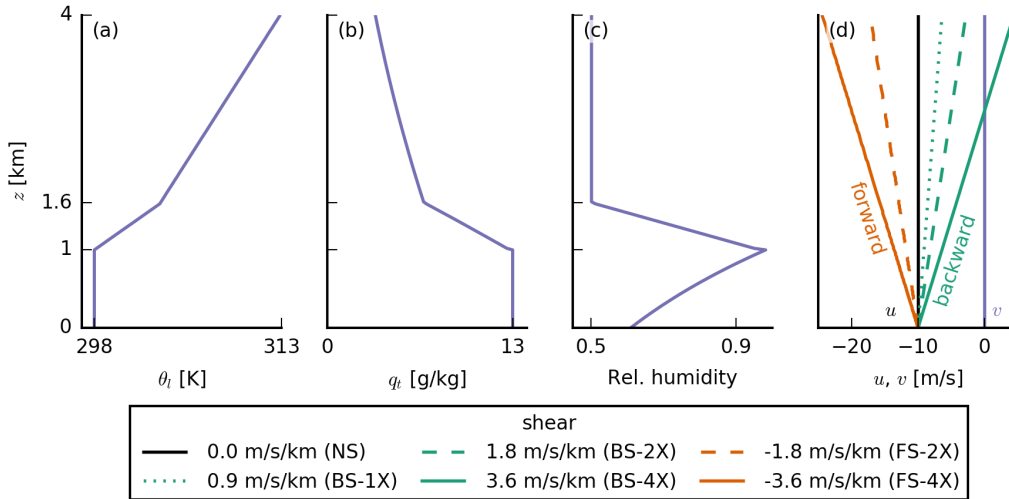


Figure 1. Initial profiles of (a) the liquid water potential temperature θ_l , (b) total water specific humidity q_t , (c) relative humidity and (d) the two wind components u and v . Purple profiles are the same in all simulations. Orange stands for forward shear (FS) and green for backward shear (BS). Same line types indicate the same amounts of absolute shear (1X, 2X, 4X). The colour coding of the different shears is the same for all other figures.

107 at a latitude of $\varphi = 15^\circ$ N (Sections 2.1–2.3). We used a domain of 50.4×50.4 km²,
 108 with a resolution of 100 m in the horizontal directions and doubly periodic boundary con-
 109 ditions. The domain top is at about 18 km and the vertical grid is non-uniform: start-
 110 ing with 10 m at the surface and increasing by a factor of 0.01 at each level to about 190 m
 111 at the domain top. In order to evaluate the effect of different surface winds and surface
 112 heat fluxes that develop under shear, we performed simulations with interactive and pre-
 113 scribed sensible and latent surface fluxes (Section 2.4). We also conducted simulations
 114 on a smaller domain (12.6×12.6 km²) where the development of cold pools and deeper
 115 clouds is less pronounced (Vogel et al., 2016).

116 2.1 Thermodynamics

117 The standard case set-up is inspired by that of Vogel et al. (2016) and Bellon and
 118 Stevens (2012), who introduced an idealised modeling framework with only a limited set
 119 of parameters that represent the large-scale flow. The initial temperature and humid-
 120 ity profiles of our simulations (Fig. 1) have a well-mixed layer of 1 km depth over a sur-
 121 face with a constant sea-surface temperature (SST) of 300 K. The mixed layer is topped

122 by a 600-m-deep inversion layer. In the free troposphere, the profile of liquid water po-
 123 tential temperature θ_l follows a constant lapse rate of 4 K/km, and the relative humid-
 124 ity is constant with height at 50 percent. We applied a constant radiative cooling rate
 125 of -2.5 K/d to θ_l (i.e. no diurnal cycle), which promotes relatively strong shallow con-
 126 vection, allowing for the development of the congestus clouds we are interested in. Com-
 127 pared to Vogel et al. (2016), we increased the domain top to 18 km to allow for deeper
 128 convection. Between 10 and 18 km, the radiative cooling is quadratically reduced to zero.
 129 The relative humidity reaches zero at about 14 km, which is also the lower boundary of
 130 the sponge layer in our LES. The θ_l lapse rate above 10 km is 8 K/km reflecting a sta-
 131 ble upper atmosphere. In all simulations, we used a single-moment ice microphysics scheme
 132 (Grabowski, 1998) and allowed for precipitation assuming a constant cloud droplet con-
 133 centration of 60 cm^{-3} .

134 2.2 Large-scale subsidence

135 Different than Vogel et al. (2016), we used a weak-temperature-gradient (WTG)
 136 assumption to calculate the subsidence profile, as the deeper congestus clouds that de-
 137 velop increasingly violate the assumption of a strongly subsiding atmosphere. Practically,
 138 the WTG method was implemented following Daleu et al. (2012): Above a reference height,
 139 we calculated the subsidence rate w_s such that it maintains the virtual potential tem-
 140 perature θ_v close to its initial (reference) profile $\theta_{v,0}$ according to

$$w_s = \frac{1}{\tau} \frac{\overline{\theta_v} - \theta_{v,0}}{\partial_z \theta_{v,0}}, \quad (1)$$

141 where the overbar indicates slab averaging, ∂_z symbolizes the vertical derivative and τ
 142 is the relaxation time scale, which can be thought of as the time scale over which den-
 143 sity anomalies are redistributed by gravity waves and thus how fast the circulation acts
 144 to counteract the heating induced by convection. We set $\tau = 1$ h, a rather short time
 145 scale that avoids the build-up of large density anomalies and unphysically high subsi-
 146 dence rates during episodes of deeper convection. WTG is not valid at levels where tur-
 147 bulence and convection effectively diffuse gravity waves. Therefore, we only apply WTG
 148 above 3 km, and below that (aligned with the bulk of the cloud layer above which cloud
 149 fraction becomes small), we linearly extrapolate w_s to zero. We also apply a nudging with
 150 a time scale of 6 h towards the initial q_t (total water specific humidity) profile in the free
 151 troposphere (above 4 km) to avoid spurious moisture tendencies.

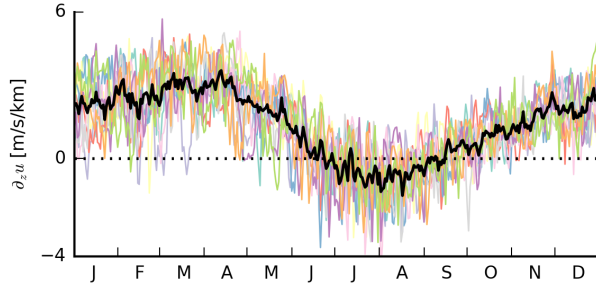


Figure 2. Time series of the amount of zonal shear between 1 and 3 km for the years 2008 to 2017 averaged over the area from 9° to 19° N and from 50° to 59° W (coloured lines). The black line is the average over all 10 years. The dotted horizontal line indicates 0 m/(s km). Data are from the ERA5 reanalysis.

152 2.3 Winds

153 The winds in our simulations are subjected to a large-scale forcing that involves
 154 only the pressure-gradient and Coriolis forces:

$$\left(\frac{du}{dt}\right)_{ls} = fv - \frac{1}{\rho} \frac{dp}{dx} = f(v - v_g), \quad (2)$$

$$\left(\frac{dv}{dt}\right)_{ls} = -fu - \frac{1}{\rho} \frac{dp}{dy} = -f(u - u_g), \quad (3)$$

155 where f is the Coriolis parameter, ρ the density, p the pressure, and u_g and v_g are the
 156 geostrophic winds. We use initial profiles of zonal and meridional winds that are equal
 157 to the imposed geostrophic wind ($u_0, v_0 = u_g, v_g$). We neglect large-scale horizontal wind
 158 advection, so that departures in the wind away from the geostrophic profiles are entirely
 159 due to the Coriolis force and the frictional force stemming from turbulence and convec-
 160 tion.

161 We based the wind profiles in our simulations on typical conditions in the trades,
 162 where vertical shear in the zonal wind component u is most common and to first order
 163 set by large-scale meridional temperature gradients through the thermal wind relation:

$$\frac{\partial u_g}{\partial z} \simeq -\frac{g}{fT} \frac{\partial T}{\partial y}, \quad (4)$$

164 where T the temperature and g the gravitational constant. In the northern hemisphere,
 165 temperature decreases poleward ($\partial_y T < 0$), so that $\partial_z u_g > 0$, which implies that winds
 166 become increasingly westerly (eastward) with height. $\partial_z u > 0$ is indeed typical for most

Table 1. Overview of the various LES experiments on a large ($50.4 \times 50.4 \text{ km}^2$) or small domain ($12.6 \times 12.6 \text{ km}^2$) and with interactive (constant SST) or fixed surface fluxes. For each set, we differentiate between runs without wind shear (NS), runs with weak (1X), medium (2X) or strong (4X) backward (BS) shear and runs with medium or strong forward (FS) shear (see also Fig. 1d).

Shear		NS	BS			FS	
			1X	2X	4X	2X	4X
acronym							
[10^{-3} s^{-1}]		0.0	+0.9	+1.8	+3.6	-1.8	-3.6
Large domain	interactive surface fluxes	✓	✓		✓		✓
	prescribed surface fluxes	✓	✓		✓		✓
Small domain	prescribed surface fluxes	✓	✓	✓	✓	✓	✓

167 of the year, as derived from daily ERA5 data (12:00 UTC) from 2008 to 2017 within 9° –
 168 19° N and 50° – 59° W (Fig. 2). In boreal summer, when the ITCZ is located in the north-
 169 ern hemisphere and meridional temperature differences within the subtropical belts are
 170 smaller, $\partial_z u$ is closer to zero or even negative. Vertical shear in the meridional wind com-
 171 ponent is close to zero year-round (not shown).

172 Further analysis of daily profiles (not shown) reveals substantial day-to-day vari-
 173 ability in the zonal wind profiles, regardless of the season, with reversals from negative
 174 to positive shear or zero shear from one day to the next, or vice versa. Forward shear
 175 (here $\partial_z u < 0$) is to some extent a frequent feature of the atmospheric flow in the trades
 176 — not only during summer. However, backward shear (here $\partial_z u > 0$) is still the most
 177 common.

178 The magnitude of shear we imposed in our simulations is not far from what we de-
 179 rived from ERA5. We ran simulations with different values of zonal shear, while setting
 180 $\partial_z v_g = 0$. The zonal wind profile has either no shear (NS, solid black line in Fig. 1d),
 181 forward shear (FS, $\partial_z u_g < 0$, orange lines) or backward shear (BS, $\partial_z u_g > 0$, green
 182 lines). The FS and BS simulations have different shear strengths ranging from $|\partial_z u_g| =$
 183 $0.9 \times 10^{-3} \text{ s}^{-1}$ (1X, dotted line in Fig. 1d) over $|\partial_z u_g| = 1.8 \times 10^{-3} \text{ s}^{-1}$ (2X, dashed
 184 lines) to $|\partial_z u_g| = 3.6 \times 10^{-3} \text{ s}^{-1}$ (4X, solid coloured lines); see also Table 1.

185 The response to shear is not entirely insensitive to the choice of advection scheme.
 186 Here, scalar and momentum advection was performed using a 5th-order advection scheme
 187 in the horizontal direction and a 2nd-order advection scheme in the vertical direction.
 188 Using a 2nd-order scheme in the horizontal further increased the differences among the
 189 shear cases (in particular under free surface fluxes), which we attribute to the fact that
 190 the 2nd-order scheme accumulates a lot of energy on the smallest length scales close to
 191 the grid size. To reduce horizontal advective errors and allow for a larger time step, the
 192 grid was horizontally translated using a velocity that is equal to the imposed wind at
 193 3 km height (Galilean transform, see e.g. Wyant et al., 2018).

194 2.4 Surface fluxes

195 The control simulations were run for two days with interactive surface fluxes, which
 196 are parametrised using standard bulk flux formulae:

$$(\psi w)_s = -C_S U_1 (\psi_1 - \psi_s), \quad (5)$$

$$u_* = \sqrt{C_M} U_1, \quad (6)$$

197 where $\psi \in \{q_t, \theta_l\}$, U is the wind speed, u_* the surface friction velocity, and the sub-
 198 scripts s and 1 stand for the surface values and values on the first model level, respec-
 199 tively. The constants C_S and C_M are the drag coefficients, and they depend on the sta-
 200 bility and on the scalar and momentum roughness lengths, which we both set to $z_0 =$
 201 1.6×10^{-4} m. The drag coefficients are computed following Monin-Obukhov similar-
 202 ity theory (as described in Heus et al., 2010). Additionally, a set of experiments was con-
 203 ducted in which the surface fluxes were kept constant.

204 3 Impact of shear on cloud- and boundary-layer evolution

205 We first focus on the differences in cloud and boundary-layer structure that have
 206 developed by the end of a two-day simulation, using twelve-hourly averaged profiles (hour
 207 36–48), unless noted otherwise.

208 3.1 Interactive surface fluxes

209 Similar to the findings of Brown (1999), who ran simulations for different wind shear
 210 on a very small domain (6.4×6.4 km²), the influence of shear (Fig. 3b–d) on the ther-
 211 modynamic structure of the boundary layer is overall marginal (Fig. 3a–b), but nonethe-

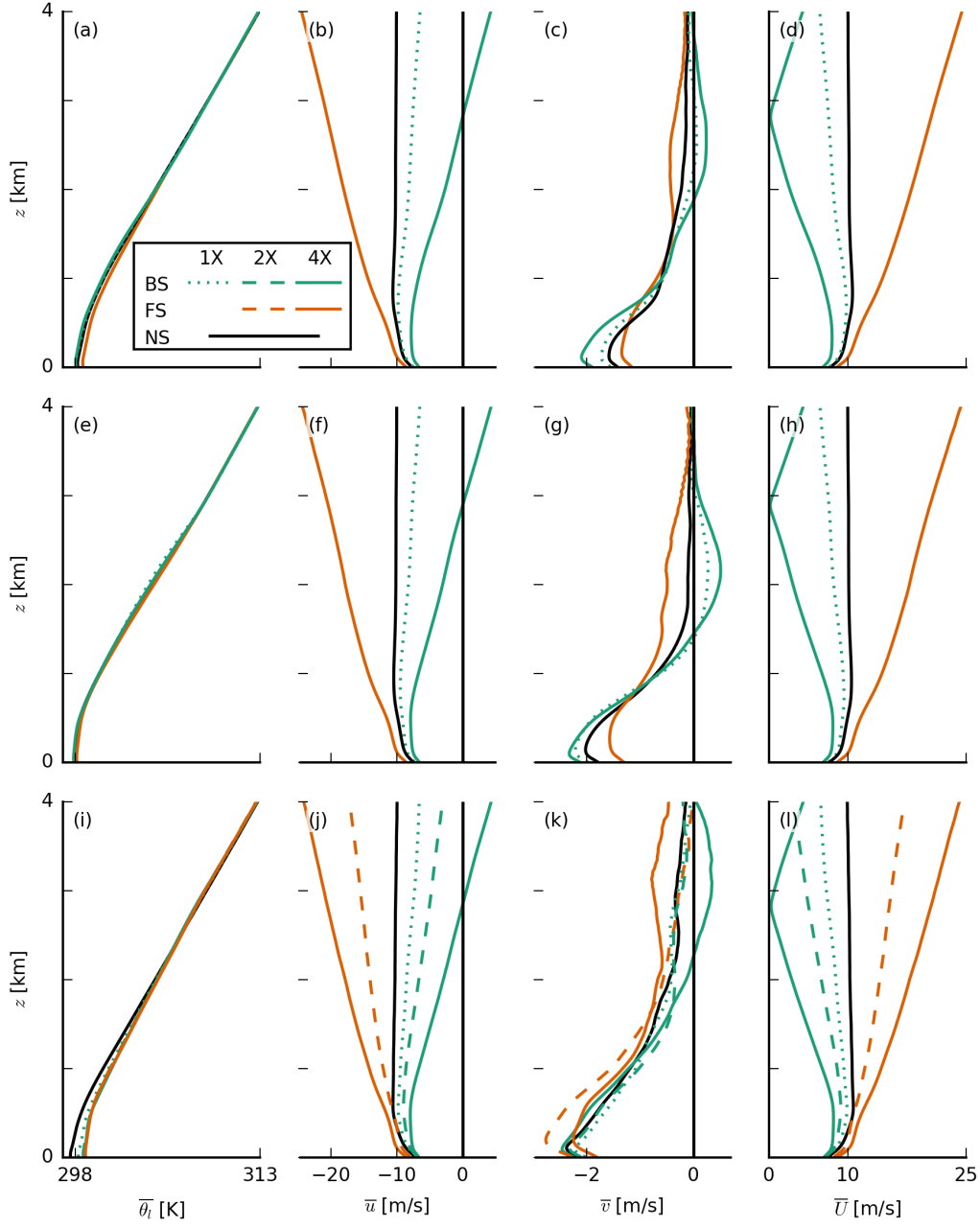


Figure 3. Slab-averaged profiles of thermodynamic quantities of the large-domain simulations with interactive surface fluxes (top row, a–d), with prescribed surface fluxes (middle row, e–h) and small-domain simulations (bottom row, i–l). Shown are averages over the last twelve hours of each simulation of (a, e, i) the liquid water potential temperature θ_l and (b, f, j) zonal, (c, g, k) meridional and (d, h, l) total wind speed, u , v and U , respectively. The line colours and types are explained in Fig. 1 and are the same in all following figures.

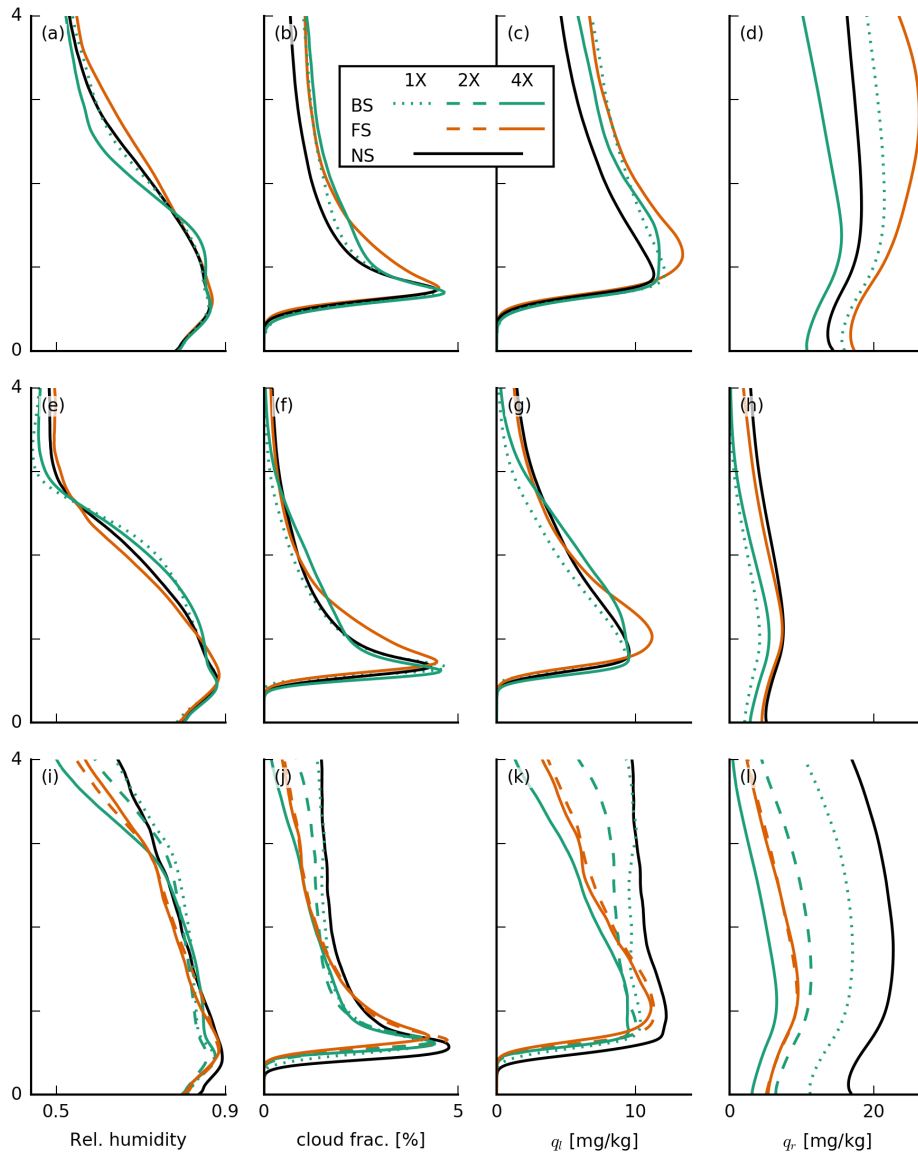


Figure 4. Slab-averaged profiles of thermodynamic quantities of the large-domain simulations with interactive surface fluxes (top row, a–d), with prescribed surface fluxes (middle row, e–h) and small-domain simulations (bottom row, i–l). Shown are averages over the last twelve hours of each simulation of (a, e, i) the relative humidity, (b, f, j) cloud fraction, (c, g, k) liquid water specific humidity q_l and (d, h, l) rain water specific humidity q_r .

212 less evident in the relative humidity (RH), cloud fraction, liquid water and rain water
 213 profiles (Fig. 4a–d). In the presence of shear, regardless of its direction, cloud fractions
 214 above cloud base (approximately 700 m) are larger. In the FS-4X case the layer above
 215 2 km is notably moister, whereas the BS-4X case has a more pronounced decrease of RH
 216 (which we interpret as the boundary-layer top) around 2 km. From strong backward to
 217 strong forward shear we thus observe a deepening of the moist layer and the disappear-
 218 ance of a pronounced hydrolapse.

219 Differences in the depth of convection are best seen from the rain water profiles (Fig. 4d)
 220 as well as the time series of average and maximum cloud-top heights (CTH), surface pre-
 221 cipitation and low cloud cover, defined as the projected cloud amount from heights up
 222 to 4 km (Fig. 5a, c, e, g). Differences in cloud tops start to be pronounced only on the
 223 second day of the simulations, but looking closer, one can see that the highest cloud tops
 224 on day one are those of the FS-4X simulations (in orange). On day two, the NS simu-
 225 lation develops the deepest clouds with even an average cloud top near 7 km, whereas
 226 clouds in the simulations with shear, regardless of its sign, remain shallower and rain less.
 227 During the final twelve hours, clouds in all simulations show a pronounced deepening,
 228 and the FS-4X case even develops deeper clouds than the NS case, as well as more rain.
 229 Because we only use a simple single-moment ice microphysics scheme here, we are cau-
 230 tious with the interpretation of the cloud field when it deepens beyond the freezing level.
 231 Instead, we wish to focus on the deepening from shallow cumuli to congestus with tops
 232 near 4 km. Apparently, shear plays a role at hindering that development, in particular
 233 under BS.

234 Figure 5 shows that the surface heat fluxes play a key role in the deepening responses.
 235 Heat fluxes diverge very early on in the simulations, whereby the largest and smallest
 236 fluxes develop for the FS-4X and BS-4X cases, respectively (Fig. 5m, o). This exempli-
 237 fies an important and perhaps often overlooked influence of wind shear. Given the same
 238 constant (geostrophic) forcing at the surface, a difference in zonal wind speeds can de-
 239 velop at the surface, due to the different zonal wind shear, which is felt near the surface
 240 through turbulent mixing, at first, and then also through the Coriolis force as the wind
 241 starts to turn (see Eq. 2 and Fig. 3b–c). These differences in surface winds (Fig. 5i) give
 242 rise to the differences in surface fluxes (see Eq. 5).

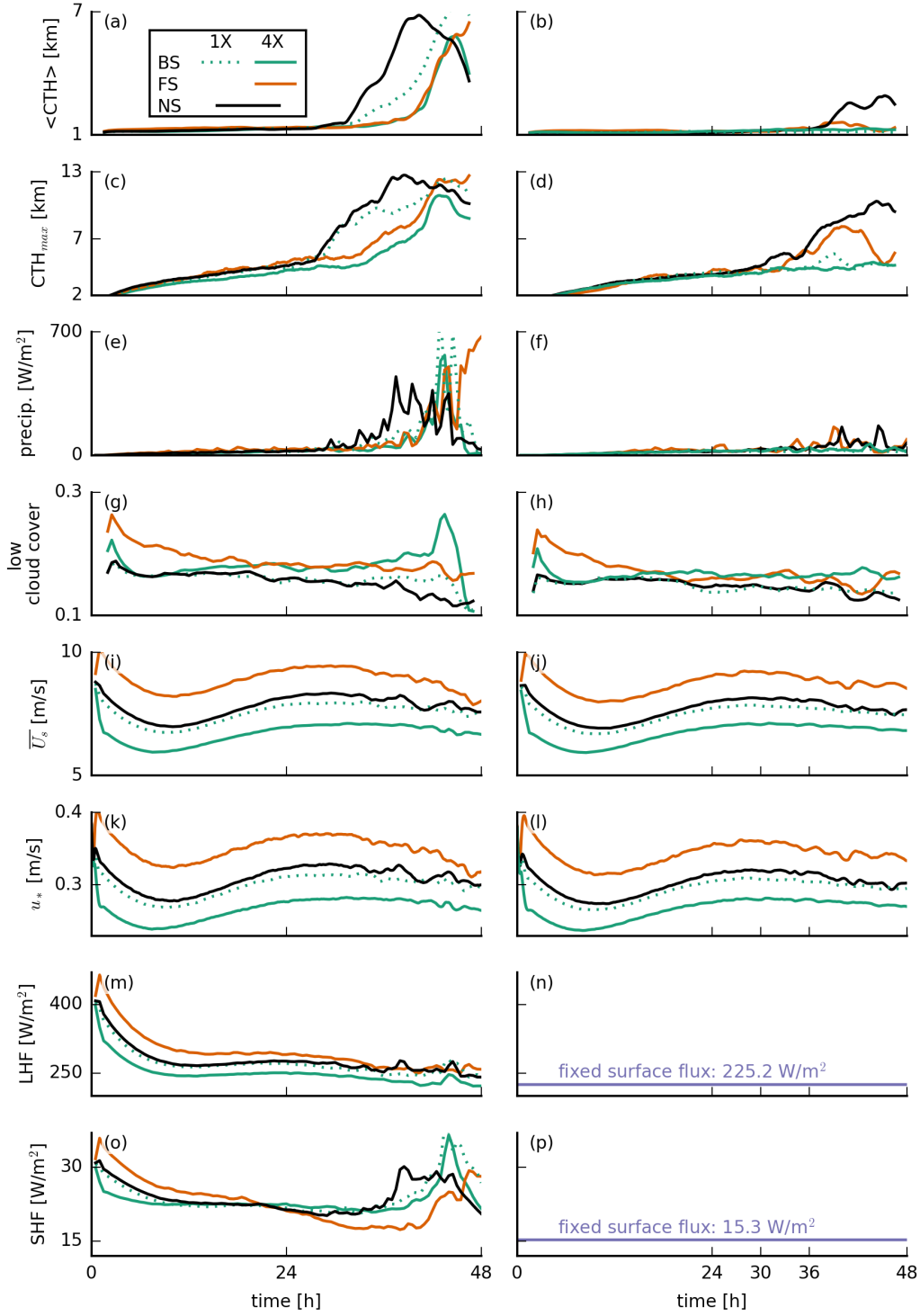


Figure 5. Time series of (a, b) the average and (c, d) the maximum cloud-top height (CTH), (e, f) the surface precipitation flux, (g, h) the low cloud cover ($z < 4$ km), (i, j) the domain-averaged total wind speed at 5 m height \bar{U}_s , (k, l) the surface friction velocity u_* , (m, n) the surface latent heat flux LHF and (o, p) the surface sensible heat flux SHF for the interactive- (left column) and prescribed-surface-flux simulations (right column).

243 As clouds deepen in all simulations during day two, the difference in surface heat
 244 fluxes becomes smaller, as downward mixing of warm and dry free tropospheric air re-
 245 duces the surface sensible heat flux while promoting the latent heat flux (Nuijens & Stevens,
 246 2012). The increase in the sensible heat fluxes in the final six hours may be attributed
 247 to precipitation and evaporative cooling of rain water in the subcloud layer (e.g. cold
 248 pools, Fig. 5e).

249 **3.2 Prescribed surface fluxes**

250 In light of these results, an important question is whether the surface fluxes are the
 251 only factor that plays a role in the development of convection, or whether shear has other
 252 more direct effects, including on the organization of clouds. Therefore, we carried out
 253 simulations with prescribed surface heat fluxes with relatively low magnitudes (namely
 254 $SHF = 15.3 \text{ W m}^{-2}$ and $LHF = 225.2 \text{ W m}^{-2}$, see the right column in Fig. 5 and
 255 second row in Figs. 3 and 4) as to minimize the development of very deep convection.
 256 Note that the surface friction (or surface momentum flux) is unchanged (Fig. 5k, l).

257 Apparently, the sensitivity of cloud deepening to shear does not change its over-
 258 all character when we prescribe the surface heat fluxes. Clouds are overall shallower with
 259 lower cloud fractions above 1 km (Fig. 4f, Fig. 5b, d), because the prescribed surface fluxes
 260 are smaller than in the interactive flux runs. But the FS-4X case still develops the largest
 261 relative humidities above the boundary layer (>2.5 km), whereas the BS-4X case has the
 262 most pronounced hydrolapse near the boundary-layer top (Fig. 4e). Again the FS-4X
 263 case tends to produce somewhat deeper clouds during day one, but falls behind the NS
 264 case on day two. The BS-4X and BS-1X cases remain even shallower.

265 From previous studies (e.g. Malkus, 1949; Neggers et al., 2003; Yamaguchi et al.,
 266 2019) it is known that shear tilts clouds and thus increases cloud cover. In our FS and
 267 BS simulations, the tilt occurs in the negative and positive x direction, respectively, which
 268 enhances the low cloud cover by 10–20 % (Fig. 5g, h). A similar increase develops within
 269 a short time also after instantaneously introducing shear into a previously non-sheared
 270 system (Fig. 6c, discussed below). Besides this expected impact on cloud cover, there
 271 are also some small differences in the cloud fraction profiles — including near cloud base,
 272 whose sensitivity has received much attention in recent climate studies (e.g. Vial et al.,
 273 2017; Bony et al., 2017). In the presence of shear, we observe a slightly larger maximum

274 cloud fraction near cloud base (500–700 m) in the simulations with prescribed surface
 275 heat fluxes (Fig. 4b, f), in line with previous studies (e.g. Brown, 1999; Yamaguchi et
 276 al., 2019). BS-4X has a higher q_t variance at these heights, which are due to a few per-
 277 cent more active cloud (not shown) and which could explain the higher cloud fraction.
 278 In the FS-4X case, the larger cloud-base cloud fraction is explained by more passive cloud
 279 (not shown).

280 3.3 Sensitivity tests on a smaller domain

281 The same difference in deepening between the shear cases can be observed when
 282 applying instantaneous perturbations to the (geostrophic) wind shear, while keeping the
 283 surface fluxes constant (Fig. 6). In these sensitivity tests, carried out on a 16-fold smaller
 284 domain (see Table 1, which is still 4 times as large as the one used by Brown (1999)) we
 285 start from the equilibrium state of the NS case after two days, and then apply a pertur-
 286 bation. We then let the system evolve for another 36 hours. Also here it is evident that
 287 when wind shear is introduced, convective deepening is prevented (Fig. 6a–b) in com-
 288 parison with how the simulation develops without a perturbation (dashed black line in
 289 Fig. 6). Even very weak shear (BS-1X, dashed green line) can effectively reduce the clouds'
 290 depth and delay cloud deepening.

291 It is worthwhile to compare the profiles of RH and cloud fraction on the small do-
 292 main (Figs. 3i–l and 4i–l) with those on the large domain. The 16-fold smaller domain
 293 leads to much higher relative humidities and cloud fractions above 2 km. This can be
 294 explained by the lack of spatial organization of shallow convection on the small domain.
 295 Increasing the domain size generally tends to organize the shallow convection into deeper
 296 and larger clusters, which leads to a shallower, warmer and drier domain. Vogel et al.
 297 (2016) found that on a larger domain the likelihood of developing a strong updraft and
 298 deep cloud increases and that larger domains support stronger and deeper updrafts by
 299 allowing them to spread their compensating subsidence over a larger area. In the absence
 300 of spatial organization on the small domain, we can observe that only the FS-4X case
 301 behaves differently compared to the large domain. This case is no longer comparably moist
 302 or even moister than the NS case and its cloud fraction and RH profile is now more in
 303 line with that of the BS-4X case. This hints at a role of spatial organization in explain-
 304 ing the response to forward shear, which we address later.

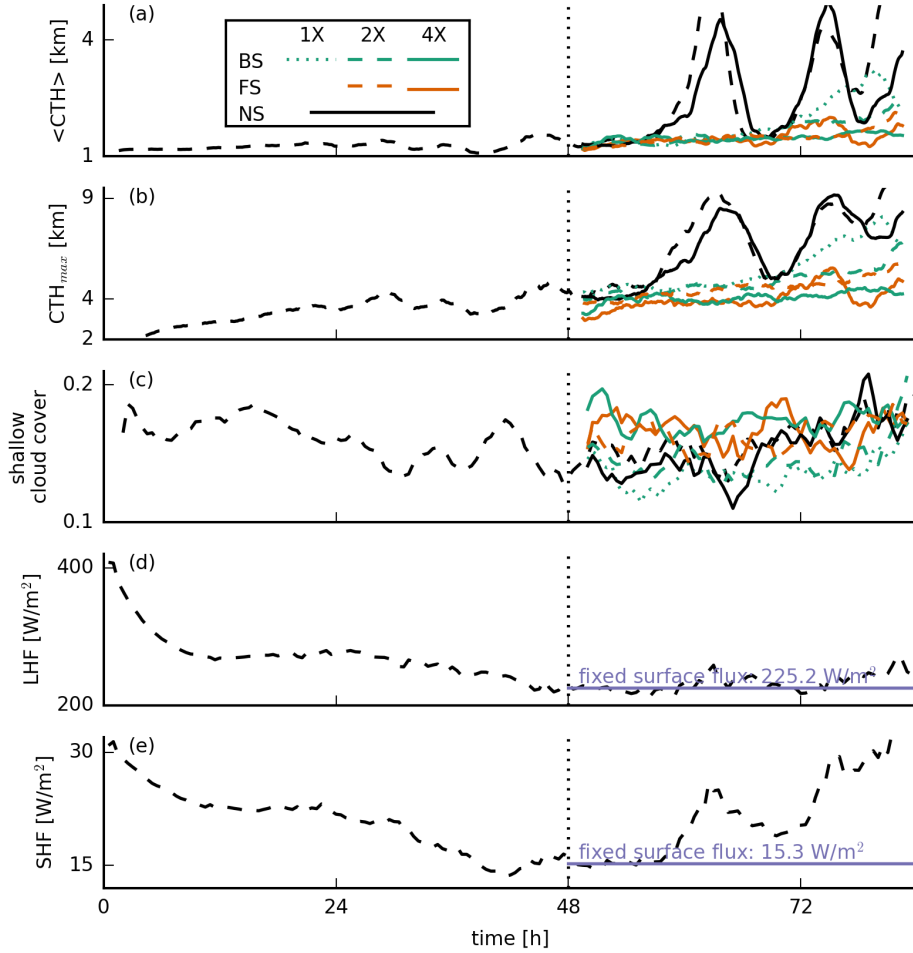


Figure 6. Time series of (a) the average and (b) the maximum cloud-top heights (CTH), (c) the low cloud cover ($z < 4$ km) and the (d) surface latent and (e) surface sensible heat fluxes for the small-domain simulations (48–84 h). In addition to the standard line types (see Fig. 1), the dashed black lines indicate a non-sheared simulation with interactive surface fluxes that is used to initialise the simulations at $t = 48$ h by perturbing the wind profiles and fixing the surface fluxes.

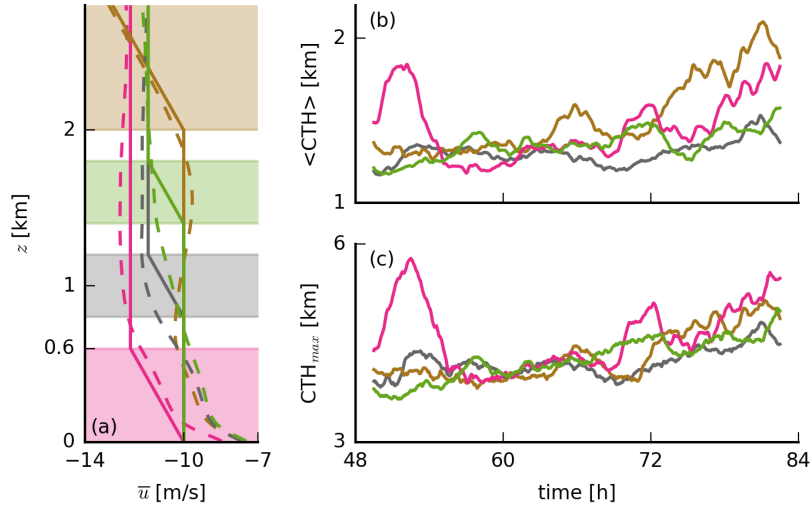


Figure 7. (a) Initial (solid lines) and slab-averaged profiles (from the last twelve hours; dashed lines) of the zonal wind u of simulations in which shear is only applied at limited height levels, as well as (b-c) the corresponding time series of the (b) average and (c) maximum cloud-top heights. Pink lines depict FS-4X shear at 0–0.6 km, grey at 0.8–1.2 km, green at 1.4–1.8 km and brown at 2–10 km.

305 Using the same experimental set-up (i.e. small domain, fixed surface fluxes and sud-
 306 den perturbation of the wind profile), we carried out some further sensitivity tests in which
 307 we applied forward shear to specific layers (Fig. 7). These simulations show that shear
 308 is particularly effective at keeping convection shallow when applied in the lower cloud
 309 layer (grey and green lines in Fig. 7), whereas shear in the subcloud layer (pink) or near
 310 cloud tops (brown) still leads to cloud deepening.

311 4 Sensitivity of convective deepening to shear

312 Overall, the previous section has shown that the presence of even weak backward
 313 shear effectively inhibits convective deepening, while forward shear only slightly weak-
 314 ens the potential to develop deeper clouds: This inhibition reveals itself as a delay (if sur-
 315 face feedbacks are present) or as a complete suppression of deepening (if surface heat fluxes
 316 are fixed). On a smaller domain, forward shear has the same strong inhibitive effect as
 317 backward shear. If not through a surface flux response, what is the mechanism through
 318 which backward shear oppresses convection, while forward shear seems to allow for cloud

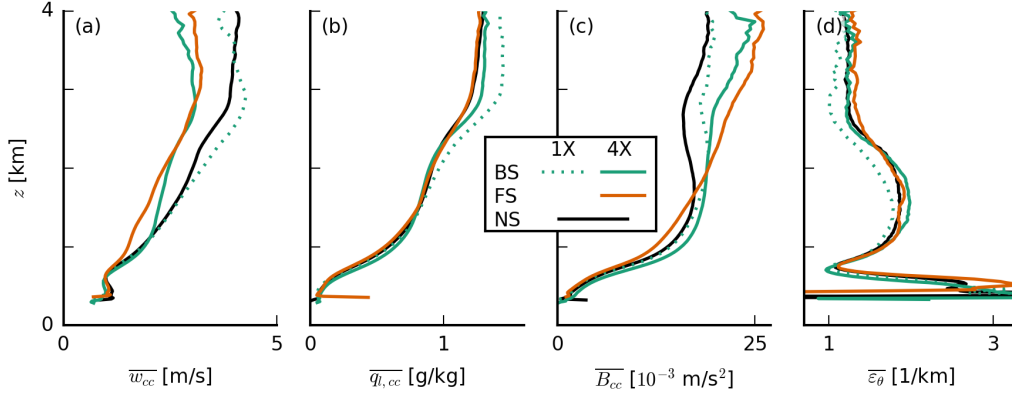


Figure 8. Slab-averaged profiles of (a) the cloud-core vertical velocity w_{cc} , (b) the cloud-core liquid water specific humidity $q_{l,cc}$, (c) the cloud-core buoyancy B_{cc} and (d) the fractional entrainment rate ε_{θ} of θ_l (averaged from 30 to 36 h of the simulations with prescribed surface fluxes).

319 deepening (on a sufficiently large domain)? Two hypotheses, borrowed from studies of
 320 deep convection, are as follows:

- 321 1. Wind shear changes the rate of entrainment, the updraft buoyancy and updraft
 322 speed: As clouds get tilted through any absolute amount of shear, they may suf-
 323 fer from more lateral entrainment and opposing pressure perturbations that limit
 324 updraft speeds and cloud vertical extent.
- 325 2. Wind shear changes the structure and organization of shallow cloud systems. For
 326 instance, forward shear helps to separate regions of updrafts and downdrafts and
 327 may therefore sustain larger subcloud circulations that continue to feed moisture
 328 into already cloudy areas. Forward shear may also interact with cold-pool fronts
 329 to force stronger updrafts.

330 To investigate these ideas, we consider only the simulations with prescribed surface fluxes
 331 and focus on the period between 30 and 36 h (unless noted otherwise). In this period,
 332 clouds first start to deepen from shallow cumulus to congestus at different rates depend-
 333 ing on shear, and the cloud field has not developed deep convection yet (cf. Fig. 5b, d).

334 4.1 Entrainment and updraft speeds

335 The FS-4X and BS-4X cases have significantly lower updraft speeds in the cloud
 336 cores ($q_l > 0$ and $\theta'_v > 0$) compared to the NS and BS-1X cases (Fig. 8a), which ap-
 337 pears key to explaining the lower cloud-top heights that develop under shear. However,
 338 the strongly sheared simulations contain nearly the same amount of cloud-core liquid wa-
 339 ter and are notably more buoyant, especially above 2 km (Fig. 8b, c). A similar picture
 340 is established if we sample on cloudy points ($q_l > 0$). Furthermore, the vertical mass
 341 flux is hardly affected by shear (not shown), as also found by Neggers et al. (2003). Buoy-
 342 ancy itself is evidently not key to explaining the weaker updrafts under shear (although
 343 it likely explains the stronger updrafts below 1 km in the BS-4X case). The relatively
 344 low buoyancy in cloud cores of the NS case (at least above 2 km) is because the envi-
 345 ronment surrounding the non-sheared clouds is warmer in terms of θ_v (not shown), be-
 346 cause clouds in that simulation are already mixing across a deeper layer (Fig. 5d), while
 347 the clouds themselves have a similar θ_v in each case. Vogel et al. (2016) also showed how
 348 quickly the thermodynamic structure of the boundary layer changes as shallow cumuli
 349 develop into cumulus congestus.

350 Using the simple entraining plume model by Betts (1975) to calculate the fractional
 351 entrainment rate ε_θ of θ_l (Fig. 8d), we find that clouds in the BS and FS cases entrain
 352 only marginally more environmental air than in the NS case if anything (also if we con-
 353 sider entrainment of q_t , not shown). This suggests that there is no larger lateral entrain-
 354 ment due to shear that could explain weaker vertical development. We also find that lat-
 355 eral entrainment plays a relatively small role in the conditionally sampled vertical-velocity
 356 budget (Appendix A).

357 The weaker cloud-core vertical velocities under shear are in line with studies of deep
 358 convection in squall lines, in particular the recent study by Peters et al. (2019) and ear-
 359 lier work by similar authors (M. D. Parker, 2010; Peters, 2016), who show that slanted
 360 updrafts are weaker than upright ones. Peters et al. (2019) decompose the vertical mo-
 361 mentum equation into four terms that describe the processes that regulate the vertical
 362 acceleration of updrafts: (1) a term associated with momentum entrainment and detrain-
 363 ment, (2) a (downward-oriented) dynamic pressure acceleration term, (3) a (downward-
 364 oriented) buoyancy pressure acceleration term and (4) a buoyancy acceleration term (which
 365 includes the entrainment of thermodynamic properties that can limit updraft buoyancy).

366 They show that shear mostly enhances the dynamic pressure perturbations, which can
 367 be interpreted as an aerodynamic lift force due to the shear-driven crossflow (perpen-
 368 dicular to the direction of ascent). Unlike the lift associated with aircraft wings, the lift
 369 in slanted thermals experiencing crossflow is directed downward. A handful of studies
 370 on the vertical-velocity budget of shallow convection have also noted a minor role of en-
 371 trainment in explaining updraft speeds (e.g. de Roode et al., 2012; Romps & Charn, 2015;
 372 Morrison & Peters, 2018; Tian et al., 2019).

373 An investigation of the vertical-velocity budget — a subject on its own as demon-
 374 strated by the aforementioned studies — goes beyond our goal, but we can get an im-
 375 pression of the importance of the pressure perturbations by sampling the vertical-velocity
 376 budget in cloudy updrafts, following de Roode et al. (2012), here included in Appendix
 377 A. We find that differences that contribute to the vertical velocity in the cloud layer are
 378 predominantly found in the pressure-gradient and buoyancy terms, whereas differences
 379 in the horizontal flux of resolved and subgrid vertical momentum across the cloud bound-
 380 aries (e.g. entrainment) are only important near cloud base (< 1 km) where other ten-
 381 dencies are small. Near cloud tops (> 2 km), updrafts in the sheared runs experience
 382 a larger negative pressure-gradient force. A quick look at the total pressure perturba-
 383 tions in x - z cross sections also confirms that pressure perturbations, especially near the
 384 slanted sides and tops of the clouds, are more pronounced under shear (not shown).

385 Overall, our results emphasise that shear keeps clouds shallower by weakening up-
 386 drafts. However, we also observe that clouds under forward shear have a tendency to get
 387 deeper than under backward shear. This is explored next.

388 4.2 Structure and organization of turbulence and clouds

389 In Fig. 9 we show a number of quantities that reveal changes to the character of
 390 the turbulence structure of the boundary layer: the domain-averaged variances of the
 391 velocity components, the turbulence kinetic energy (TKE), the skewness S and third cen-
 392 tral moment of the vertical velocity $\overline{w'^3}$ and finally the zonal and meridional momentum
 393 fluxes. Velocity variances are clearly enhanced in the FS-4X case, where the vertical gra-
 394 dient in wind speed between the surface and cloud tops — the shear — is largest (cf. Fig 3f-
 395 h). Consequently, TKE and the momentum fluxes are larger, in agreement with Brown

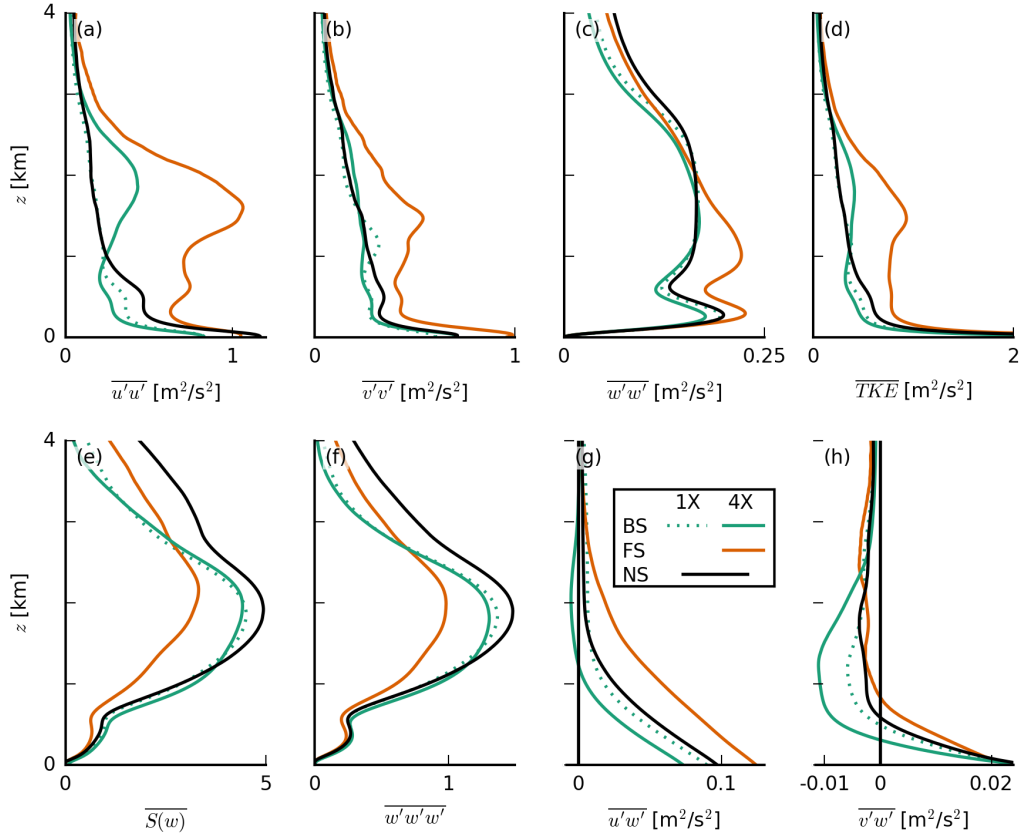


Figure 9. Slab-averaged profiles of the resolved variances of (a) the zonal wind speed $u'u'$, (b) the meridional wind speed $v'v'$ and (c) the vertical velocity $w'w'$, (d) the turbulence kinetic energy (TKE), (e) the skewness $S(w)$, (f) the third moment $w'w'w'$ of the vertical velocity and (g) the zonal and (h) the meridional momentum fluxes, $u'w'$ and $v'w'$, respectively (averaged from 30 to 36 h of the simulations with prescribed surface fluxes).

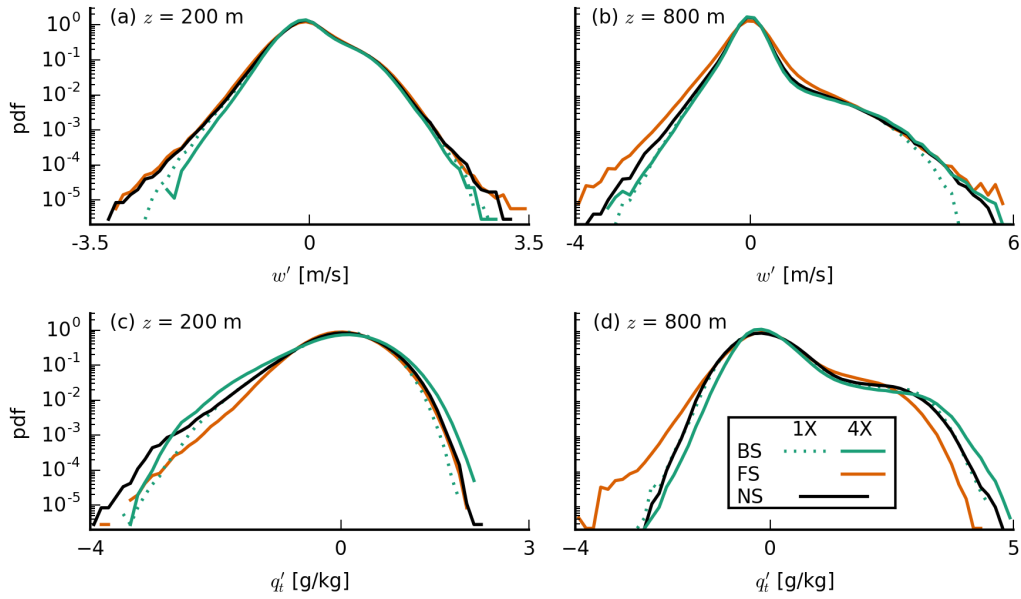


Figure 10. Probability density functions of the vertical velocity w (top) and the total water specific humidity deviations q'_t (bottom) at constant heights of (left) $z = 200$ m and (right) $z = 800$ m (averaged from 30 to 36 h of the simulations with prescribed surface fluxes).

396 (1999). Momentum fluxes at the surface are also largest for the FS-4X case, leading to
 397 a larger surface friction (see also Fig. 5i, j) and larger surface-layer shear.

398 Several authors have noted that convection can transition from a closed-cell struc-
 399 ture to roll structures due to shear (e.g. Sykes & Henn, 1989; Khanna & Brasseur, 1998;
 400 Salesky et al., 2017). A parameter that controls this transition is the ratio of the sur-
 401 face friction velocity u_* to the convective velocity scale w_* (Sykes & Henn, 1989) or equiv-
 402 alently the ratio of the Obukhov length and the boundary-layer height. While the ex-
 403 act value of u_*/w_* at which the transition takes place depends on other properties of the
 404 flow (different studies report values between 0.27 and 0.65), low values are clearly asso-
 405 ciated with cellular convection and high values with roll structures (Fedorovich & Conzemius,
 406 2008; Salesky et al., 2017). In our simulations, u_*/w_* has rather low values, which do
 407 not differ greatly among the various shear cases (ranging from about 0.30 for BS-4X to
 408 0.37 for FS-4X), indicating that convection is mainly buoyancy- and not shear-driven in
 409 all our simulations.

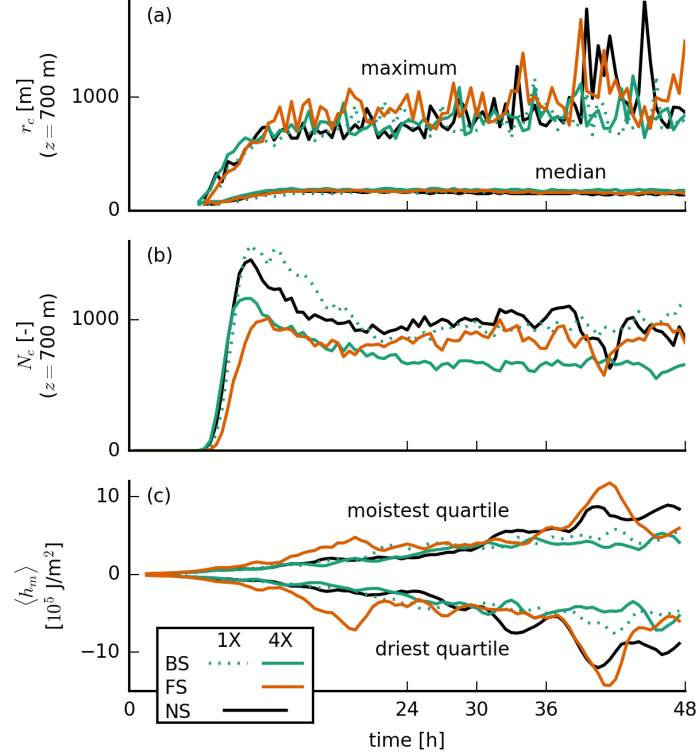


Figure 11. Time series of (a) the median and maximum cloud radius r_c at $z = 700$ m, (b) the number of clouds N_c at that height and (c) the vertically integrated moist static energy anomalies $\langle h_m \rangle$ in the moistest and the driest quartiles of 12.6×12.6 km² blocks for the simulations with prescribed surface fluxes.

410 The skewness of the vertical velocity $S(w) = \overline{w'^3} / \overline{w'^2}^{3/2}$, which is a measure for
 411 the asymmetry of the vertical velocity distribution, is reduced with FS. This is primar-
 412 ily caused by the reduction in the advection of vertical velocity variance, $\overline{w'^3}$, due to on
 413 average weaker updrafts into the cloud layer (Fig. 8a). The variance of w instead is larger
 414 under FS-4X (Fig. 9c). Although the PDFs of w at 200 m and at 800 m (near cloud base)
 415 in Fig. 10a–b are overall very similar, the FS-4X case has notably stronger updrafts as
 416 well as stronger downdrafts (tails of the PDF). This might be a signature of the down-
 417 drafts being separated from the updraft regions. Because the FS-4X case also has the
 418 largest absolute amount of wind shear across the subcloud layer, it has the largest posi-
 419 tive (anticlockwise) vorticity. These results suggest that instead of narrow updrafts closely
 420 surrounded by subsidence, the FS-4X case develops stronger ascent and descent in sep-
 421 arated branches of a circulation that enhances moisture transport into cloudy areas.

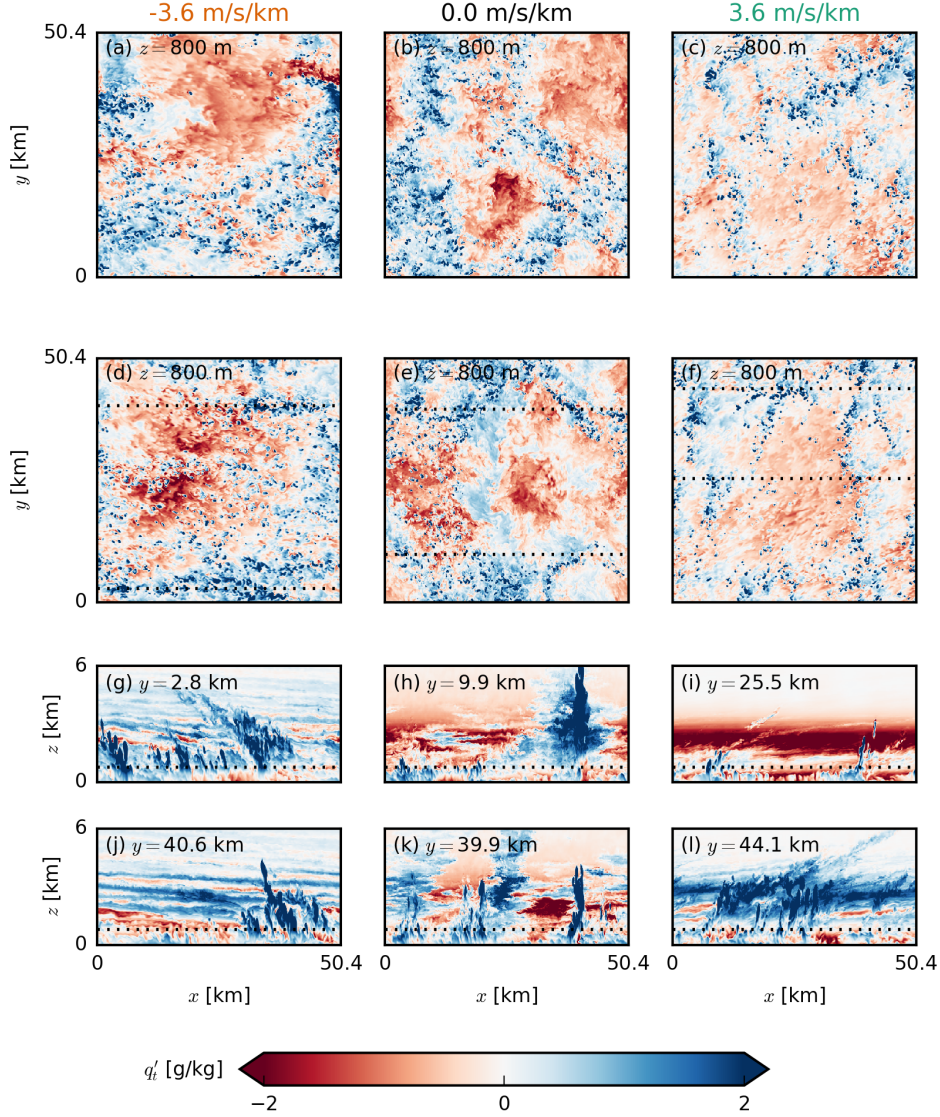


Figure 12. Snapshots of the LES domains of FS-4X (left), NS (centre) and BS-4X (right) exhibiting typical characteristics in the late stages of the simulations with prescribed surface fluxes. The top two rows (a–f) show horizontal x - y cross sections at two times ($t = 39.0$ h and $t = 46.5$ h) near cloud base ($z = 800$ m) of the deviations from the mean of the total water specific humidity q'_t . The bottom two rows (g–l) show corresponding vertical x - z cross sections from the lowest 6 km of the domain of the latter of the two times (d–f). The horizontal dotted lines indicate the position of the respective other cross sections.

422 Indeed, the FS-4X case has the largest amount of domain-averaged liquid water and
 423 cloud fraction between 800 m and 1.5 km on both small and large domains (Fig. 4f, g,
 424 j, k) and larger relative humidities just above cloud base (Fig. 4e, i), even though cloud
 425 base is on average higher than for the BS and NS cases. By analysing the mean and max-
 426 imum cloud radii and the number of clouds, we also find that the FS-4X case develops
 427 the fewest but the largest clouds (Fig. 11a, b), whereas the NS case has more numerous
 428 smaller clouds, similar to findings by Yamaguchi et al. (2019).

429 The formation or aggregation of larger clouds is also evident from the moisture field.
 430 Figure 11c shows deviations of the vertically integrated moist static energy within blocks
 431 of $12.6 \times 12.6 \text{ km}^2$ compared to the domain mean, and compares the moistest and the
 432 driest quartiles of the domain (in terms of total water path), which is a common mea-
 433 sure for self-aggregation (Bretherton & Blossey, 2017). This reveals that during the first
 434 24 h the strongest moistening of the moist regions and strongest drying of the dry re-
 435 gions takes place in the FS-4X cases. Furthermore, snapshots of the moisture field (Fig. 12)
 436 show that large patches of high or low moisture are less common in the simulations with
 437 backward shear compared to the other cases.

438 After the first day of simulation when precipitation increases, cold-pool effects might
 439 play an additional role in organizing the cloud and moisture field. The cold-pool bound-
 440 aries may interact with the environmental shear in the subcloud layer to trigger stronger
 441 force-lifted updrafts under FS (e.g. Li et al., 2014). The FS and BS cases also have a
 442 different wind speed distribution within the cold pools (Fig. 13). Whereas the BS case
 443 reveals the typical diverging flow with a strong easterly current left from the cold pool
 444 center and relatively stronger westerly winds towards the right, the FS case has much
 445 stronger easterly winds throughout. This may signify a role of downward momentum trans-
 446 port as well. The role of cold pool–shear interaction is the subject of a follow-up study.

447 5 Conclusions

448 In this paper, we have used idealised large-eddy simulations initialized and forced
 449 with a geostrophic wind that is equal at the surface, but has a different vertical profile
 450 (vertical wind shear). We showed that vertical wind shear influences the depth and char-
 451 acteristics of shallow cumulus convection, and thereby the depth and structure of the trade-
 452 wind layer. Even weak vertical shear in the zonal wind component can retard the growth

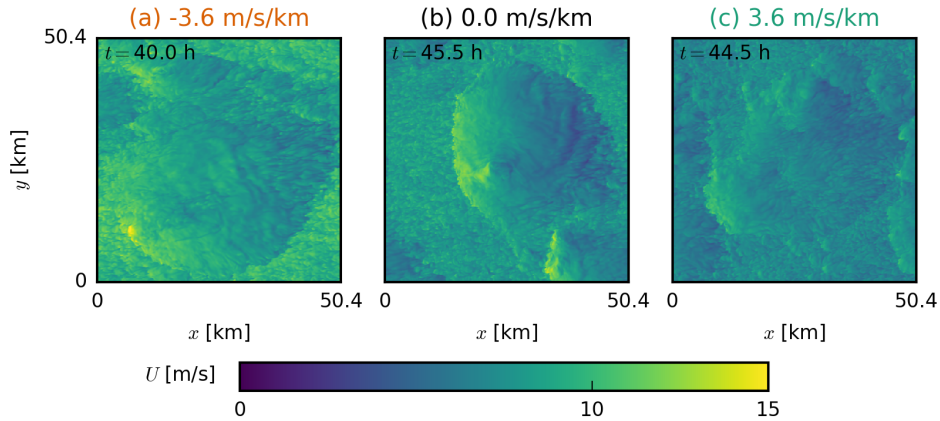


Figure 13. Snapshots of the LES domains of (a) FS-4X, (b) NS and (c) BS-4X exhibiting typical characteristics of the total wind speed U in the late stages of the simulations with prescribed surface fluxes. Shown are horizontal x - y cross sections at $z = 5$ m.

453 of cumulus clouds, in particular when the shear vector is directed against the mean wind
 454 direction (backward shear). Furthermore, we have shown that shear increases the cloud
 455 fraction — an effect that has been of major interest in recent climate studies (e.g. Vial
 456 et al., 2017; Bony et al., 2017).

457 Backward shear, whereby surface easterlies become upper westerlies, is typical for
 458 the winter trades, presumably because this season has a larger meridional temperature
 459 gradient between the equator and subtropics. Simulations with interactive surface fluxes
 460 reveal that backward shear can slow down vertical cloud development. Under backward
 461 shear, mean cloud tops remain near 2 km for at least 36 hours of simulation, at which
 462 point the simulations without (imposed) shear have developed clouds with mean tops
 463 near 7 km. Given the same geostrophic wind forcing at the surface, and in absence of
 464 horizontal wind advection, the weakest surface winds develop under backward shear. This
 465 relative reduction of the wind is caused by vertical momentum transport: Under back-
 466 ward shear relatively weaker wind speeds are mixed towards the surface compared to a
 467 no-shear or a forward-shear wind profile. This in turn leads to weaker surface heat fluxes.

468 Weak shear and forward shear (easterlies become stronger with height) are not un-
 469 common during boreal winter, even if they are more typical for boreal summer when the
 470 ITCZ and deep convection shift northward. The vertical development of clouds under

471 forward shear is also delayed, but not as much as with backward shear, because simu-
472 lations with forward shear develop the strongest surface winds and (initially) the largest
473 surface heat fluxes.

474 To elucidate more direct effects of vertical shear, we repeated the simulations with
475 prescribed surface heat fluxes. These show that the presence of shear in the cloud layer,
476 regardless of its sign, limits updraft speeds, in line with studies of deep convection that
477 have shown shear to inhibit convective development (e.g. Peters et al., 2019). Entrain-
478 ment appears to play a minor role in setting the weaker updrafts (e.g. de Roode et al.,
479 2012; Romps & Charn, 2015; Morrison & Peters, 2018; Tian et al., 2019). Instead, larger
480 downward-oriented pressure perturbations under both forward and backward shear ap-
481 pear to weaken vertical accelerations.

482 In addition, shear changes the turbulence structure of the subcloud layer. Though
483 our simulations remain buoyancy-driven and do not develop roll structures or cloud streets,
484 forward shear develops stronger updrafts and downdrafts, a moister layer near cloud base
485 with larger cloud fraction, fewer but larger cloud clusters and more moisture aggrega-
486 tion. Forward shear maintains the largest absolute amount of shear in the sub-cloud layer,
487 which leads to a larger background vorticity and separates regions with updrafts from
488 regions with downdrafts. This may develop a stronger subcloud circulation with sustained
489 regions of ascending motion that feed moisture into areas of clouds. The larger cloud clus-
490 ters can become deeper, as they do in the first day of simulation under forward shear,
491 but are ultimately limited by weaker updraft speeds.

492 As clouds remain shallower under backward shear, the moistening of the cloud layer
493 is more pronounced and the top of the cloud layer is marked by a steeper decrease in hu-
494 midity, as is typical near the trade-wind inversion (e.g. Riehl et al., 1951). The moister
495 subcloud and cloud layer, as well as a stronger inversion, will lead to more cloudiness.
496 Therefore, we may argue that the trade winds themselves help to set the trade-wind in-
497 version and thus that backward shear is a crucial ingredient in defining the typical trade-
498 wind-layer structure.

499 **Appendix A Impact of shear on the vertical-velocity budget**

500 To study a difference in the forcing acting on the vertical velocity of cloudy updrafts
501 in simulations with and without shear we follow the method by de Roode et al. (2012)

502 who applied the top-hat approach by Siebesma and Cuijpers (1995) to compute the con-
 503 ditionally sampled vertical-velocity budget in DALES:

$$\frac{\partial w_c}{\partial t} = \underbrace{\frac{g(\theta_{v,c} - \bar{\theta}_v)}{\theta_0}}_B - \underbrace{\left[\frac{\partial \pi}{\partial z} \right]_c}_P + \underbrace{2\Omega \cos \varphi u_c}_C - \underbrace{\frac{1}{2} \frac{\partial w_c^2}{\partial z}}_A - \underbrace{\frac{1}{\sigma_c} \frac{\partial \sigma_c \overline{w'' w''^c}}{\partial z}}_{S_p} - \underbrace{\frac{\epsilon_w w_c^2}{1 - \sigma_c}}_E \quad (\text{A1})$$

504 where the subscript c stands for conditional sampling (here: on cloudy updrafts, i.e. $q_l >$
 505 0 and $w > 0$), g the gravitational acceleration, θ_v the virtual potential temperature,
 506 θ_0 a reference temperature, π the modified pressure, Ω Earth's angular velocity, φ the
 507 latitude, σ the area fraction and ϵ_w the fractional entrainment rate of w . The modified
 508 pressure π is defined as

$$\pi = \frac{1}{\rho_0} (p - \bar{p}_h) + \frac{2}{3} e, \quad (\text{A2})$$

509 where ρ_0 is a constant reference density, p the pressure, p_h the hydrostatic pressure and
 510 e the subgrid-scale TKE. The latter is included because in DALES, $\frac{2}{3}e$ is subtracted from
 511 the subgrid momentum flux to simplify its computation; to compensate for this, the term
 512 is added back to the pressure (Heus et al., 2010). Preliminary tests show, however, that
 513 the subgrid TKE contribution to the conditionally sampled pressure term is small and
 514 insensitive to shear (not shown). The tendency on the l.h.s. of Eq. A1 is calculated di-
 515 rectly from the LES. Averaged over six hours (30 to 36 h) it is close to zero. This ten-
 516 dency closely matches the sum of the terms on the r.h.s., which represent the buoyancy
 517 acceleration (B), the vertical pressure gradient (P), the Coriolis force (C), the vertical
 518 advection (A), the subplume vertical advection (S_p), and the lateral entrainment E .

519 Above 1 km, in the cloud layer, the production of vertical velocity from positive
 520 buoyancy B is largely balanced by a sink of vertical velocity due to the pressure gradi-
 521 ent P , followed by a smaller sink from advection A . The subplume term S_p is close to
 522 zero in the cloud layer, and C is also small (negative). The lateral entrainment term E
 523 is small yet positive, counter to the conventional idea that entrainment is contributing
 524 negatively to cloud updraft quantities. This unexpected sign of the diagnosed lateral en-
 525 trainment rate might be due to detrainment of descending cloud air across the edges (Heus
 526 & Jonker, 2008), whereas the top-hat approach assumes that updraft cloud air is detrained.
 527 As discussed in detail in de Roode et al. (2012), the conditionally sampled entrainment
 528 here does not only include the horizontal flux of resolved and subgrid vertical momen-
 529 tum across the cloud boundaries, but also so-called Leibniz terms that result from the
 530 temporal change in vertical velocity due to changes in the sampling set (for example, cloud

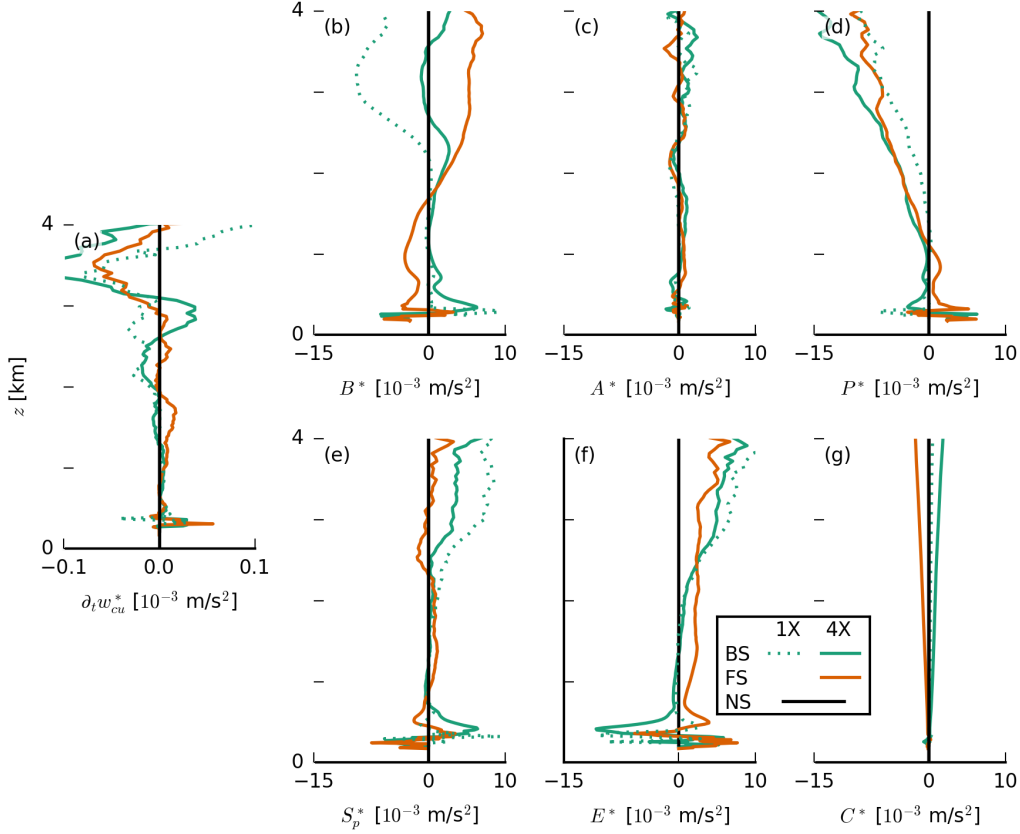


Figure A1. Slab-averaged profiles (averaged from 30 to 36 h of the simulations with prescribed surface fluxes) of the terms of the cloudy-updraft vertical-velocity budget (Eq. A1) plotted as differences from the NS case (indicated by the asterisks).

531 parcels that are vertically accelerated and disappear from the cloud ensemble at the next
 532 time step, see their Eq. A9). In any case, E tends to be smaller than the B and P terms.

533 To explain how different forcings under shear can contribute to differences in the
 534 updraft speeds, Fig. A1 shows these budget terms as deviations from the NS case. Pos-
 535 itive values indicate a stronger positive contribution to updraft speed (or a smaller neg-
 536 ative contribution). In particular, above 1 km, the FS and BS cases have a larger neg-
 537 ative P contribution (Fig. A1d), which is present at the same altitude where we see slower
 538 updraft speeds in the presence of shear (Fig. 8a). The differences in P are balanced mostly
 539 by differences in E (in the BS-4X case) or B (in the FS-4X case). The latter result from
 540 the different development of environmental temperature and humidity, as discussed in
 541 Section 4.1 and shown in Fig. 8c. The NS case with its strongest updrafts develops the

542 deepest clouds and thus the warmest boundary layer, which reduces B , leading to a bal-
543 ance in the budget over six hours. It thus appears that initial differences in updraft speeds
544 develop due to differences in pressure gradients under shear, which are maintained through-
545 out the simulation, as a balance with the buoyancy force is established. There is also an
546 interesting difference in diagnosed lateral entrainment (Fig. A1f), which appears larger
547 positive in FS-4X. We therefore cannot conclude that entrainment differences do not play
548 a role (in establishing different updraft speeds). However, because the Leibniz terms can
549 have a significant magnitude, this method of diagnosing the vertical-velocity budget may
550 not be the best to address that difference further.

551 **Acknowledgments**

552 We would like to thank Chris Bretherton and Bjorn Stevens for stimulating discussions
553 as well as two anonymous reviewers for their comments that greatly improved the manuscript.
554 This project has received funding from the European Research Council (ERC) under the
555 European Union’s Horizon 2020 research and innovation programme (Starting grant agree-
556 ment no. 714918). ERA5 data were generated using Copernicus Climate Change Ser-
557 vice Information. Neither the European Commission nor ECMWF is responsible for any
558 use that may be made of the Copernicus information or data in this publication. DALES
559 is open-source software, which is distributed under the terms of the GNU GPL version
560 3. The exact version of the code as well as the input files used in this work are available
561 via <https://doi.org/10.5281/zenodo.3714862>.

562 **References**

- 563 Asai, T. (1964). Cumulus Convection in the Atmosphere with Vertical Wind Shear.
564 *Journal of the Meteorological Society of Japan. Ser. II*, 42(4), 245–259.
- 565 Bellon, G., & Stevens, B. (2012). Using the Sensitivity of Large-Eddy Simulations
566 to Evaluate Atmospheric Boundary Layer Models. *Journal of the Atmospheric*
567 *Sciences*, 69(5), 1582–1601. doi: 10.1175/JAS-D-11-0160.1
- 568 Betts, A. K. (1975). Parametric Interpretation of Trade-Wind Cumulus Budget
569 Studies. *Journal of the Atmospheric Sciences*, 32(10), 1934–1945. doi: 10
570 .1175/1520-0469(1975)032<1934:PIOTWC>2.0.CO;2
- 571 Bony, S., & Dufresne, J.-L. (2005). Marine boundary layer clouds at the heart of
572 tropical cloud feedback uncertainties in climate models. *Geophysical Research*

- 573 *Letters*, 32(20). doi: 10.1029/2005GL023851
- 574 Bony, S., Stevens, B., Ament, F., Bigorre, S., Chazette, P., Crewell, S., . . . Wirth,
575 M. (2017). EUREC4A: A Field Campaign to Elucidate the Couplings Be-
576 tween Clouds, Convection and Circulation. *Surveys in Geophysics*. doi:
577 10.1007/s10712-017-9428-0
- 578 Bony, S., Stevens, B., Held, I. H., Mitchell, J. F., Dufresne, J.-L., Emanuel, K. A.,
579 . . . Senior, C. (2013). Carbon Dioxide and Climate: Perspectives on a Sci-
580 entific Assessment. In G. R. Asrar & J. W. Hurrell (Eds.), *Climate Science*
581 *for Serving Society* (pp. 391–413). Dordrecht: Springer Netherlands. doi:
582 10.1007/978-94-007-6692-1_14
- 583 Bretherton, C. S., & Blossey, P. N. (2017). Understanding Mesoscale Ag-
584 gregation of Shallow Cumulus Convection Using Large-Eddy Simulation.
585 *Journal of Advances in Modeling Earth Systems*, 9(8), 2798–2821. doi:
586 10.1002/2017MS000981
- 587 Brown, A. R. (1999). Large-eddy simulation and parametrization of the effects of
588 shear on shallow cumulus convection. *Boundary-Layer Meteorology*, 91(1), 65–
589 80.
- 590 Brueck, M., Nuijens, L., & Stevens, B. (2015). On the Seasonal and Synoptic
591 Time-Scale Variability of the North Atlantic Trade Wind Region and Its Low-
592 Level Clouds. *Journal of the Atmospheric Sciences*, 72(4), 1428–1446. doi:
593 10.1175/JAS-D-14-0054.1
- 594 Daleu, C. L., Woolnough, S. J., & Plant, R. S. (2012). Cloud-Resolving Model
595 Simulations with One- and Two-Way Couplings via the Weak Temperature
596 Gradient Approximation. *Journal of the Atmospheric Sciences*, 69(12), 3683–
597 3699. doi: 10.1175/JAS-D-12-058.1
- 598 de Roode, S. R., Siebesma, A. P., Jonker, H. J. J., & de Voogd, Y. (2012).
599 Parameterization of the Vertical Velocity Equation for Shallow Cumu-
600 lus Clouds. *Monthly Weather Review*, 140(8), 2424–2436. doi: 10.1175/
601 MWR-D-11-00277.1
- 602 Fedorovich, E., & Conzemius, R. (2008). Effects of wind shear on the atmospheric
603 convective boundary layer structure and evolution. *Acta Geophysica*, 56(1),
604 114–141. doi: 10.2478/s11600-007-0040-4
- 605 Grabowski, W. W. (1998). Toward Cloud Resolving Modeling of Large-Scale Trop-

- 606 ical Circulations: A Simple Cloud Microphysics Parameterization. *Journal of*
 607 *the Atmospheric Sciences*, 55(21), 3283–3298. doi: 10.1175/1520-0469(1998)
 608 055(3283:TCRMOL)2.0.CO;2
- 609 Heus, T., & Jonker, H. J. J. (2008). Subsiding Shells around Shallow Cumulus
 610 Clouds. *Journal of the Atmospheric Sciences*, 65(3), 1003–1018. doi: 10.1175/
 611 2007JAS2322.1
- 612 Heus, T., van Heerwaarden, C. C., Jonker, H. J. J., Siebesma, P. A., Axelsen, S.,
 613 van den Dries, K., . . . Vilà-Guerau de Arellano, J. (2010). Formulation
 614 of the Dutch Atmospheric Large-Eddy Simulation (DALES) and overview
 615 of its applications. *Geoscientific Model Development*, 3(2), 415–444. doi:
 616 10.5194/gmd-3-415-2010
- 617 Hildebrand, P. H. (1998). Shear-Parallel Moist Convection over the Tropical Ocean:
 618 A Case Study from 18 February 1993 TOGA COARE. *Monthly Weather Re-*
 619 *view*, 126(7), 1952–1976. doi: 10.1175/1520-0493(1998)126(1952:SPMCOT)2.0
 620 .CO;2
- 621 Hill, G. E. (1968). On the orientation of cloud bands. *Tellus*, 20(1), 132–137. doi:
 622 10.3402/tellusa.v20i1.9936
- 623 Khanna, S., & Brasseur, J. G. (1998). Three-Dimensional Buoyancy- and Shear-
 624 Induced Local Structure of the Atmospheric Boundary Layer. *Journal of the*
 625 *Atmospheric Sciences*, 55(5), 710–743. doi: 10.1175/1520-0469(1998)055(0710:
 626 TDBASI)2.0.CO;2
- 627 Klein, S. A., Hall, A., Norris, J. R., & Pincus, R. (2017). Low-Cloud Feedbacks
 628 from Cloud-Controlling Factors: A Review. *Surveys in Geophysics*, 38(6),
 629 1307–1329. doi: 10.1007/s10712-017-9433-3
- 630 Koren, I., Remer, L. A., Altaratz, O., Martins, J. V., & Davidi, A. (2010). Aerosol-
 631 induced changes of convective cloud anvils produce strong climate warming.
 632 *Atmos. Chem. Phys.*, 10(10), 5001–5010.
- 633 LeMone, M. A., & Pennell, W. T. (1976). The Relationship of Trade Wind Cu-
 634 mulus Distribution to Subcloud Layer Fluxes and Structure. *Monthly Weather*
 635 *Review*, 104(5), 524–539. doi: 10.1175/1520-0493(1976)104(0524:TROTWC)2
 636 .0.CO;2
- 637 Li, Z., Zuidema, P., & Zhu, P. (2014). Simulated Convective Invigoration Processes
 638 at Trade Wind Cumulus Cold Pool Boundaries. *Journal of the Atmospheric*

- 639 *Sciences*, 71(8), 2823–2841. doi: 10.1175/JAS-D-13-0184.1
- 640 Malkus, J. S. (1949). Effects of wind shear on some aspects of convection.
 641 *Transactions, American Geophysical Union*, 30(1), 19. doi: 10.1029/
 642 TR030i001p00019
- 643 Malkus, J. S. (1963). Cloud Patterns over Tropical Oceans. *Science*, 141(3583), 767–
 644 778. doi: 10.1126/science.141.3583.767
- 645 Morrison, H., & Peters, J. M. (2018). Theoretical Expressions for the Ascent Rate of
 646 Moist Deep Convective Thermals. *Journal of the Atmospheric Sciences*, 75(5),
 647 1699–1719. doi: 10.1175/JAS-D-17-0295.1
- 648 Neggers, R. A., Jonker, H. J., & Siebesma, A. P. (2003). Size statistics of cumulus
 649 cloud populations in large-eddy simulations. *Journal of the Atmospheric Sci-*
 650 *ences*, 60(8), 1060–1074. doi: 10.1175/1520-0469(2003)60<1060:SSOCCP>2.0
 651 .CO;2
- 652 Nuijens, L., & Stevens, B. (2012). The Influence of Wind Speed on Shallow Ma-
 653 rine Cumulus Convection. *Journal of the Atmospheric Sciences*, 69(1), 168–
 654 184. doi: 10.1175/JAS-D-11-02.1
- 655 Park, S.-B., Böing, S., & Gentine, P. (2018). Role of Surface Friction on Shallow
 656 Nonprecipitating Convection. *Journal of the Atmospheric Sciences*, 75(1),
 657 163–178. doi: 10.1175/JAS-D-17-0106.1
- 658 Parker, D. J. (1996). Cold pools in shear. *Quarterly Journal of the Royal Meteorolo-*
 659 *gical Society*, 122(535), 1655–1674. doi: 10.1256/smsqj.53508
- 660 Parker, M. D. (2010). Relationship between System Slope and Updraft Intensity
 661 in Squall Lines. *Monthly Weather Review*, 138(9), 3572–3578. doi: 10.1175/
 662 2010MWR3441.1
- 663 Pastushkov, R. S. (1975). The effects of vertical wind shear on the evolution of
 664 convective clouds. *Quarterly Journal of the Royal Meteorological Society*,
 665 101(428), 281–291. doi: 10.1002/qj.49710142811
- 666 Peters, J. M. (2016). The Impact of Effective Buoyancy and Dynamic Pressure Forc-
 667 ing on Vertical Velocities within Two-Dimensional Updrafts. *Journal of the At-*
 668 *mospheric Sciences*, 73(11), 4531–4551. doi: 10.1175/JAS-D-16-0016.1
- 669 Peters, J. M., Hannah, W., & Morrison, H. (2019). The Influence of Vertical Wind
 670 Shear on Moist Thermals. *Journal of the Atmospheric Sciences*, 76(6), 1645–
 671 1659. doi: 10.1175/JAS-D-18-0296.1

- 672 Riehl, H., Yeh, T. C., Malkus, J. S., & La Seur, N. E. (1951). The north-east trade
673 of the Pacific Ocean. *Quarterly Journal of the Royal Meteorological Society*,
674 *77*(334), 598–626.
- 675 Robe, F. R., & Emanuel, K. A. (2001). The Effect of Vertical Wind Shear on Ra-
676 diative–Convective Equilibrium States. *Journal of the Atmospheric Sciences*,
677 *58*(11), 1427–1445. doi: 10.1175/1520-0469(2001)058<1427:TEOVWS>2.0.CO;
678 2
- 679 Romps, D. M., & Charn, A. B. (2015). Sticky Thermals: Evidence for a Dominant
680 Balance between Buoyancy and Drag in Cloud Updrafts. *Journal of the Atmo-*
681 *spheric Sciences*, *72*(8), 2890–2901. doi: 10.1175/JAS-D-15-0042.1
- 682 Rotunno, R., Klemp, J. B., & Weisman, M. L. (1988). A Theory for Strong, Long-
683 Lived Squall Lines. *Journal of the Atmospheric Sciences*, *45*(3), 463–485. doi:
684 10.1175/1520-0469(1988)045<0463:ATFSSL>2.0.CO;2
- 685 Salesky, S. T., Chamecki, M., & Bou-Zeid, E. (2017). On the Nature of
686 the Transition Between Roll and Cellular Organization in the Convec-
687 tive Boundary Layer. *Boundary-Layer Meteorology*, *163*(1), 41–68. doi:
688 10.1007/s10546-016-0220-3
- 689 Sathiyamoorthy, V., Pal, P. K., & Joshi, P. C. (2004). Influence of the Upper-
690 Tropospheric Wind Shear upon Cloud Radiative Forcing in the Asian
691 Monsoon Region. *Journal of Climate*, *17*(14), 2725–2735. doi: 10.1175/
692 1520-0442(2004)017<2725:IOTUWS>2.0.CO;2
- 693 Siebesma, A. P., & Cuijpers, J. W. M. (1995). Evaluation of Parametric Assump-
694 tions for Shallow Cumulus Convection. *Journal of the Atmospheric Sciences*,
695 *52*(6), 650–666. doi: 10.1175/1520-0469(1995)052<0650:EOPAFS>2.0.CO;2
- 696 Sykes, R. I., & Henn, D. S. (1989). Large-Eddy Simulation of Turbulent Sheared
697 Convection. *Journal of the Atmospheric Sciences*, *46*(8), 1106–1118. doi: 10
698 .1175/1520-0469(1989)046<1106:LESOTS>2.0.CO;2
- 699 Thorpe, A. J., Miller, M. J., & Moncrieff, M. W. (1982). Two-dimensional con-
700 vection in non-constant shear: A model of mid-latitude squall lines. *Quarterly*
701 *Journal of the Royal Meteorological Society*, *108*(458), 739–762. doi: 10.1002/
702 qj.49710845802
- 703 Tian, Y., Kuang, Z., Singh, M. S., & Nie, J. (2019). The Vertical Momentum
704 Budget of Shallow Cumulus Convection: Insights From a Lagrangian Perspec-

- 705 tive. *Journal of Advances in Modeling Earth Systems*, *11*(1), 113–126. doi:
706 10.1029/2018MS001451
- 707 Vial, J., Bony, S., Stevens, B., & Vogel, R. (2017). Mechanisms and Model Diversity
708 of Trade-Wind Shallow Cumulus Cloud Feedbacks: A Review. *Surveys in Geo-*
709 *physics*, *38*(6), 1331–1353. doi: 10.1007/s10712-017-9418-2
- 710 Vogel, R., Nuijens, L., & Stevens, B. (2016). The role of precipitation and
711 spatial organization in the response of trade-wind clouds to warming.
712 *Journal of Advances in Modeling Earth Systems*, *8*(2), 843–862. doi:
713 10.1002/2015MS000568
- 714 Weisman, M. L., & Rotunno, R. (2004). “A Theory for Strong Long-Lived Squall
715 Lines” Revisited. *Journal of the Atmospheric Sciences*, *61*, 361–382.
- 716 Wyant, M. C., Bretherton, C. S., & Blossey, P. N. (2018). The Sensitivity of
717 Numerical Simulations of Cloud-Topped Boundary Layers to Cross-Grid
718 Flow. *Journal of Advances in Modeling Earth Systems*, *10*(2), 466–480. doi:
719 10.1002/2017MS001241
- 720 Yamaguchi, T., Feingold, G., & Kazil, J. (2019). Aerosol-Cloud Interactions in
721 Trade Wind Cumulus Clouds and the Role of Vertical Wind Shear. *Jour-*
722 *nal of Geophysical Research: Atmospheres*, *124*(22), 12244–12261. doi:
723 10.1029/2019JD031073